Thermal analysis and FTIR study of 4-*n*-hexadecyloxybenzoic acid (16OB)

Arkadiusz Rudzki[1] · Janusz Chruściel[1] · Sławomir Zalewski[1] · Wojciech Zając[2]

Abstract

We have carried out phase polymorphism studies of 4-*n*-hexadecyloxybenzoic acid (16OB) in temperature range: from 10 to 150 °C with the use of Differrential Scanning Calorimeter, Thermal Microscopic Polarization and Transmitted Light Intensity. 16OB is a liquid crystal which has smectic C phase (SmC) and rich polymorphism in solid phase. Particularly interesting is one of the transitions in solid state possessing characteristic clear exothermic effect (during heating cycle) which is associated with the transition between the metastable and stable phases. Fourier transform infrared spectroscopy as a function of temperature was used to analyze changes in the nature of hydrogen bonds. The exact analysis of effects shows an existence of the metastable phases. The stable and metastable phases differ from each other in the structure made of hydrogen bonds.

Keywords Thermal analysis · Exo-energetic effect · Hydrogen bonds · Metastable phases

Introduction

N-alkoxybenzoic acids are mesogenic compounds, they are characterized by the presence of: nematic phase (N) (for *n* from 3 to 6 carbon atoms in the alkyl chain), nematic and smectic C (SmC) phases (for *n* = 7–14) and only SmC phase for *n* > 14 [1]. Alkoxybenzoic acids are most often found in the form of dimers due to intermolecular hydrogen bonds. The nature of these bonds has been and is widely studied by various groups of physicists, both in pure acids and in mixtures with their participation [2–8]. Alkoxybenzoic acids are a group of compounds that is interesting for both cognitive and numerous applications. The applicability of these compounds is related to their use as intermediates in the syntheses of liquid crystal materials [e.g. 9–13], materials of biological significance [e.g. 14], as components of liquid crystal mixtures [e.g. 7, 15, 16] and as independent research materials [17]. Most of the studies presented in the literature concern acids with an average alkoxy chain length. For

our research, we chose hexadecyloxybenzoic acid (16OB), which is a monomorphic liquid crystal having an enantiotropic SmC phase. Compounds having SmC phases can be desirable ingredients in mixtures with chiral additives that generate an SmC* phase over a wide temperature range. The 16OB acid also turned out to be interesting due to the phenomenon of the phase transition in the solid phase, the exo-energetic transition. The exo-energetic effect occurs when a substance is cooled from a liquid phase to a solid phase characterized by a slow crystallization rate (e.g. transition to a glassy phase). Heating of such a phase causes the accumulation of thermal energy in it, the release of which leads to an anomaly (cold crystallization) below the melting point. In some materials, the glass transition effect is observed not during cooling, but during heating. The first materials in which the cold crystallization effect were observed were polymers [18–22]. Further studies proved that the tendency to accumulate energy before the melting point is also shown by other materials, such as: liquid crystals [23–26], ionic liquids [27], some organic materials [e.g. 28, 29] and complexes of organic compounds with metals e.g. [30]. Research on monomolecular crystalline materials provided some clues as to the structure of these compounds [23–30]. In order for thermal energy to be stored, the molecule should contain flexible groups, which increases the degree of mobility and the possibility of creating numerous isomers. Even a slight change in the geometry of the isomer can determine the

✉ Arkadiusz Rudzki
  arkadiusz.rudzki@uph.edu.pl

1 Faculty of Science, Siedlce University of Natural Sciences and Humanities, 3 Maja Street No. 54, 08-110 Siedlce, Poland

2 Institute of Nuclear Physics, Polish Academy of Sciences, 31-342 Kraków, Poland

possibility of cold crystallization. It is also desirable that the liquid phase consists of several phases with varying degrees of ordering, which disturbs the homogeneity of the system. The 16OB acid molecule contains a long flexible element in the form of a 16-carbon terminal chain and a rigid element which is a benzene ring connected by an ether bond with an alkyl chain and a carboxyl group. The easy formation of intermolecular hydrogen bonds, especially in the open form, causes that the structure composed of many 16OB molecules creates flexible, spatial systems resembling polymer structures. The formation of such structures promotes the agglomeration of thermal energy, the release of which is visible in the DSC diagrams in the form of an exo-energetic effect.

The aim of our work is to determine the acid phase polymorphism (16OB) during heating and cooling, with particular emphasis on the dynamics of the exo-energetic transition. FTIR spectroscopy as a function of temperature changes provided us with information about the nature of intermolecular hydrogen bonds in individual 16OB phases.

Fourier transform infrared (FTIR) spectroscopy shows the changes occurring at the molecular level that accompany phase changes. The changes affect the dynamics of vibrations and are observable as changes in the parameters of the absorption bands: wave number, full-width and half-width (FWHM), area and height. These changes are observed in infrared spectra measured successively as a function of temperature [31].

In alkoxybenzoic acids, carboxyl groups (HO–C=O) play a major role in the formation of hydrogen bonds. The region of stretching vibrations of the carbonyl group (C=O), which can form hydrogen bonds with the –OH group of the adjacent molecule or with hydrogen atoms in the aromatic core, is particularly sensitive. Changes in the dynamics of vibrations accompanying the formation and breaking of hydrogen bonds in alkoxybenzoic acids observed in FTIR spectra were widely discussed [4, 5].

Experimental

Material

We obtained the 16OB acid in our laboratory in accordance with the procedure generally used for the preparation of alkoxybenzoic acids, [e.g. 36]. We bought substrates for the synthesis (hexadecyl bromide, p-hydroxybenzoic acid, methanol, ethanol, toluene, potassium bromide and other necessary compounds from Sigma-Aldrich. The purity of the final compound was examined by thin layer chromatography (Merck aluplates, Kieselgel 60 F254) using ethyl acetate-methylene chloride 1: 1), and confirmed by FTIR and 1H NMR.

Synthesis

A solution of 4-hydroxybenzoic methyl ester (0,11 mol), potassium carbonate (0,15 mol) and 25 mL butanon-2 heated to dissolve the 4-hydroxybenzoic acid methyl ester, then hexadecyl bromide (0,12 mol) was added and the mixture was heated under reflux for 10 h. the reaction mixture was poured into ice water, stirred well and filtered. The obtained product was hydrolyzed in a solution: 25 mL water and 150 mL ethanol containing 28 g of KOH at reflux temperature et 5 h, after which the mixture was cooled to room temperature and acidified with HCl (4 M). The precipitate was filtered, washed with water and $3 \times$ recrystallized from ethanol to give the pure product 4-heksadecyloxybenzoic acid white solid, 89% yield. Phase transition temperatures: 99,8 °C (Cr-SmC), 131,5 °C (SmC-I); IR: ν HO···H (2563–2728 cm^{-1}), νOH (3473 cm^{-1}), νC=O (1688 cm^{-1}); ^{1}H NMR (500 MHz, CDCl$_3$) δ 8.00 (d, 2 Ar–H), 7.03 (d, 2 Ar–H), 4.04 (t, 2H OCH$_2$), 1.94–1.69 (m, 2H), 1.53–1.31 (m, 26H), 0.89 (t, 3H).

DFT calculations

Quantum-chemical calculations of DFT were performed using TURBOMOLE v7.3. [35]. For a single 16OB molecule and its dimer, quantum-chemical DFT calculations were performed with the base def2-TZVPPD set for all atoms [36] with the B3-LYP functional [37], applying corrections for D4 dispersion [38]. The B3LYP functional is a hybrid (correlation/exchange) functional known to be one of the best and certainly the most used. Semi-empirical dispersion corrections are important in the case of large, flexible molecules, e.g. liquid rod-like crystals, where weak non-covalent intramolecular interactions of medium and long range affect the conformational state of the molecules, as well as vibration frequencies, especially those in which there are labile hydrogen atoms. In the case of the dimer, two functionalities B3-LYP and PBE-3 h were used. The optimized dimer (with both methods) is not perfectly linear, the angle between the chains is approx. 3.2 degrees, and the angle of mutual twisting of the rings—approx. 1 degree. The 3.2 degree angle can be a little bigger, at the cost of a really minimal energy change, well below the thermal energy. Thus, the dimer exhibits oscillation at a pair of hydrogen bonds that tolerate such changes in angle well.

Fig. 1 The most energetically advantageous conformations of 16OB: **a** single molecule and **b** dimer system with the use of various functional

(a)

(b)

(c)
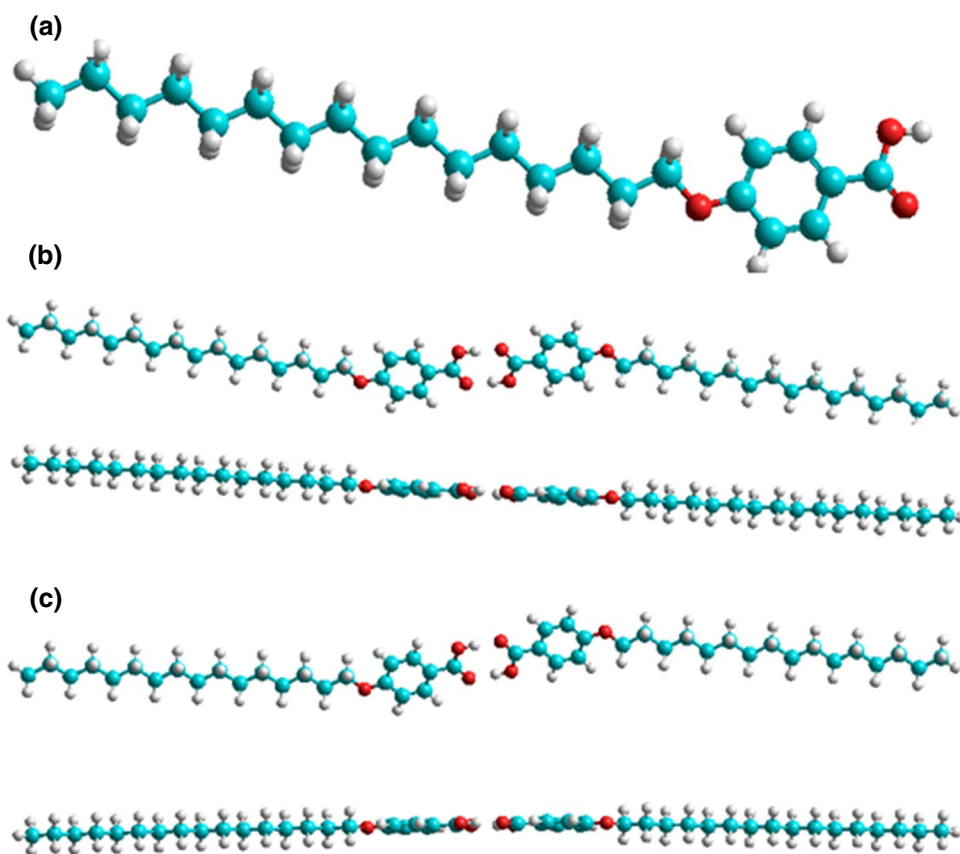
This is an important feature of this type of dimer, the longer the chain, the less stable the dimer. The most energetically beneficial conformations are shown in Fig. 1.

Methods

Phase polymorphism studies in temperature range: − 10 °C to + 150 °C were executed using scanning calorimeter DSC Mettler Toledo 822e and polarizing microscope Optatech equipped with the heating stage THMSE 600 LINKAM. A first order lambda plate was used for microscopic studies. Transform light intensity (TLI) measurements were made in the system: source of light, polarizing microscope, detector and recorder. Light after passing through sample fell on photodiode and the voltage of this photodiode was recorded as a function of temperature and time. Precise description of TLI measurement set was presented in work [39]. The sample was placed in a 6 μm glass cell for the TLI and POM studies. All measurements were obtained with rate 2° min⁻¹.

Temperature FTIR spectra were recorded on MAGNA IR 760 NICOLET spectrometer equipped with the heating stage THMSE 600 LINKAM. Temperature was controlled with the process controller TMS 93 LINKAM with an accuracy of ± 0,1 °C. IR spectra were made with resolution 1 cm⁻¹

using 64 co-added scans. Samples were formed into KBr pellets.

Results

The calorimetric and temperature IR studies were performed by the following chronology:

(a) Measurement in the temperature range of − 10 °C to + 150 °C for a fresh sample of 16OB.
(b) Repeated measurement in the temperature range − 10 °C to + 150 °C.
(c) Measurement for the sample previously melted within the temperature range from -10 °C to + 120 °C (melting the sample into SmC phase).
(d) Repeat the cycle c).
(e) The next measurement was in the range from − 10 °C to + 80 °C (in the area of the solid phase without fusing)
(f) Repeat the cycle e)

For microscopic investigations (POM and TLI), cycles b)–f) were performed. It was impossible to measure a 'fresh'
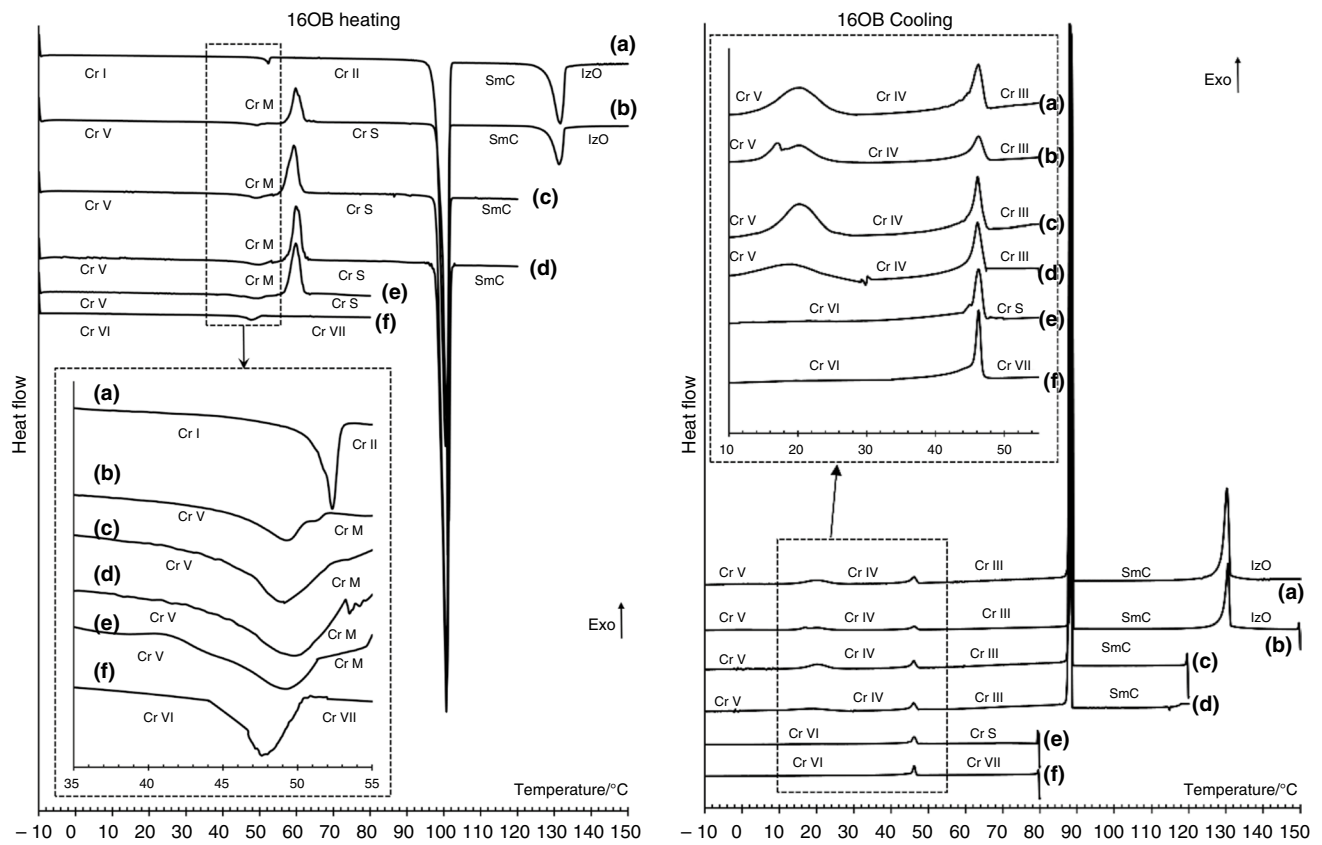
Fig. 2 DSC curves of 16OB obtained from cycles **a**–**f** during heating (left side) and during cooling (right side)

Table 1 Temperatures (T_p) of phase transitions and enthalpies (ΔH) obtained in calorimetric measurements in a)–f) cycles

Cycle	Process	Phase transition	T_p/°C	ΔH/J g^{-1}	Cycle	Process	Phase transitions	T_p/°C	ΔH/J g^{-1}
a)	Heating	CrI-CrII	52.3	− 1.30	d)	Heating	CrV-CrM	48.9	− 2.33
		CrII-SmC	99.8	− 141.27			CrM-CrS	59.3	22.00
		SmC-Izo	131.5	− 28.89			CrS-SmC	99.8	− 141.15
	Cooling	Izo-SmC	130.4	24.38		Cooling	SmC-CrIII	89.2	82.47
		SmC-CrIII	89.4	81.55			CrIII-CrIV	46.1	2.33
		CrIII-CrIV	46.3	1.98			CrIV-CrV	20.1	4.05
		CrIV-CrV	20.7	2.90	e)	Heating	CrV-CrM	49.8	− 2.48
b)	Heating	CrV-CrM	49.2	− 2.10			CrM-CrS	59.9	22.02
		CrM-CrS	59.8	24.90		Cooling	CrS-CrVI	46.2	1.45
		CrS-SmC	100.3	− 143.44	f)	Heating	CrVI-CrVII	47.7	− 2.05
		SmC-Izo	131.2	− 29.59		Cooling	CrVII-CrVI	46.3	2.14
	Cooling	Izo-SmC	130.6	25.53					
		SmC-CrIII	89.4	83.48					
		CrIII-CrIV	46.2	2.25					
		CrIV-CrV	20.4	4.53					
c)	Heating	CrV-CrM	49.1	− 1.71					
		CrM-CrS	59.9	21.84					
		CrS-SmC	100.0	− 141.04					
	Cooling	SmC-CrIII	89.4	81.55					
		CrIII-CrIV	46.1	1.88					
		CrIV-CrV	19.4	2.87					

sample (cycle a)) because the acid had to be melted to fill the measuring cell.

Calorimetric studies

Phase situation of 16OB obtained during heating and cooling is presented on Fig. 2. The temperature of phase transitions and the corresponding enthalpies is included in the Table 1. We introduced the numbering of the crystalline phases in the order of their occurrence, starting with heating from − 10 °C, and cooling the sample.

DSC measurements show that heating a "fresh" crystalline sample shows no exo-energetic effect. There is one low-energy CrI–CrII transition in the solid phase at 52.3 °C. At 99.8 °C, the CrII phase passes into the SmC phase, which at 131.5 °C passes into the isotropic phase. Cooling the isotropic phase generates the following transitions: I—SmC (130.4 °C), SmC–CrIII (89.4 °C), CrIII–CrIV (46.3 °C), CrIV–CrV (20.7 °C) (cycle a, Fig. 2). Reheating the sample from a temperature of—10 °C (cycle b) leads to a transition between the crystalline phases with a clear exo-energy effect at 58.9 °C ($\Delta H = 24$ J g^{-1}), so the following phase situation is recorded during heating: low energy transition ($\Delta H = 2.1$ J g^{-1}) CrV-CrM (49.2 °C), CrM-CrS (exo-energy transition at 58.9 °C), CrS-SmC (100.3 °C); SmC-I (131.2 °C).

This behaviour of the solid phase in 16OB may indicate that during cooling of the isotropic phase (cycle a) there are difficulties with the alignment of the conformers due to the interaction of long chains, which could freeze some conformations of the molecule. Heating the phase marked as CrV causes its glass transition at 49.2 °C and then cold crystallization at 59.8 °C to the phase which we have marked as CrS. The observed thermal behavior of the 16OB sample is similar to that of polymers [e.g. 19] and others in materials with a typical glassy phase [e.g. 41, 42].

Cooling the isotropic phase generates the following phase transitions (cycle b): I—SmC (130.6 °C), SmC-CrIII (89.4 °C), CrIII–CrIV (46.2 °C), CrIV–CrV (20.4 °C), phase situation is the same as in the cooling down of cycle a). In order to check whether the temperature to which the sample is heated has an influence on the changes in the crystalline phase, subsequent measurement cycles (cycle c–f) were performed.

In two measuring cycles (cycle c, d) the sample was heated to the SmC phase (temp. 120 °C) and then the SmC phase was cooled. It turned out that it is enough to melt the sample without reaching the refining point for the exo-energetic effect to occur. The phase situation during heating and cooling in these cases was analogous to that in cycles b).

In the next cycle e), the sample was heated to 80 °C, (20 °C above the exo-energetic transition). When cooling the sample from 80 °C, only one low-energy transition ($\Delta H = 1$ J g^{-1}) is visible between the crystalline phases at

46.2 °C. In the heating cycle (cycle f) of the sample from − 10 °C to 80 °C, one pass is visible at 47.7 °C without exo-energetic effect. Recooling the sample (cycle f) reproduces the situation in cycle e).

The above measurements show that the sufficient condition to obtain the exo-energetic effect (cold crystallization) in 16OB is the substance melting, moving to the SmC phase. Isotropization is not necessary.

The influence of the rate of temperature changes on the change of the parameters of phase transitions and the range of phase occurrence was noticed. We performed another measurement with different heating and cooling rates (1, 2, 3, 5, 10° min^{-1} in the range of 0–150 °C), (cycle g) We presented the results in the form of a table (Table 2) and graphs in Fig. 3.

Two phase transitions depend on the rate of changes in the heating/cooling rate of the sample: the first is related to the exothermic effect (CrM→CrS transition) occurring during heating (Fig. 3b), and the second occurs in the cooling cycle at a temperature of about 20 °C, CrIV→CrV transition (Fig. 3d). The remaining phase transitions are practically independent of the rate of temperature changes (Fig. 3a, c) and minor differences in transition temperatures are within the experimental error. For the CrM→CrS transformation, an increase in the transition temperature was observed with the increase in the rate of temperature changes (Fig. 3b), and the increase was linear. The range of CrM phase occurrence slightly increases: from 8.8 deg. at a rate of 1 K min^{-1} to 10.5 deg. at a rate of 10 K min^{-1}. The extrapolated transition temperature for a rate of 0 K min^{-1} is 57 °C. On the other hand, for the CrIV→CrV transformation, a decrease in the transition temperature is visible with the increase in the rate of temperature changes (Fig. 3d), and the decrease is polynomial. The extrapolated transition temperature at 0 K min^{-1} is 25.8 °C.

In order to determine the effect of time on the stability of the 16OB phase situation, the sample after measurements was left at room temperature for 17 days, and then the measurement cycle was carried out at the rate of 5 K min^{-1}. (Fig. 4). The DSC curve shows that during heating from room temperature to 125 °C (to the SmC phase), the thermal situation of the sample is analogous to the g cycle (5 K min^{-1}) (Table 2), with the transitions characterized by lower enthalpy changes. The value of ΔH of the exo-energetic transition is lower by 15.4 J g^{-1} than in the cycle g), which may suggest temporary disappearance of the "exo" effect. Cooling the SmC phase causes the same situation as in cycle g, Table 2).

The sample was left at room temperature for another 40 days, and then a full DSC measurement cycle was carried out at 5 K min^{-1}. (heating to 125 °C and cooling to 0 °C). The obtained situation is analogous to that in cycle a) (Fig. 2, Table 1). No exo-energetic effect was observed.

Table 2 Phase transition temperatures (T_p) and enthalpy changes (ΔH) for 16OB in DSC measurements made with different temperature change rates

Rate of temperature change	Process	Phase transition	T_p/°C	ΔH/J g^{-1}	Rate of temperature change	Process	Phase transition	T_p/°C	ΔH/J g^{-1}
1 K min^{-1}	Heating	CrV-CrM	49.2	− 2.54	5 K min^{-1}	Heating	CrV-CrM	49.5	− 2.14
		CrM-CrS	58.0	22.81			CrM-CrS	63.6	25.45
		CrS-SmC	99.9	− 142.63			CrS-SmC	100.3	− 141.40
		SmC-Izo	131.3	− 28.38			SmC-Izo	131.5	− 26.30
	Cooling	Izo-SmC	130.7	26.32		Cooling	Izo-SmC	130.1	28.84
		SmC-CrIII	89.4	82.83			SmC-CrIII	89.44	84.09
		CrIII-CrIV	46.2	2.32			CrIII-CrIV	46.14	2.59
		CrIV-CrV	24.1	3.74			CrIV-CrV	15.71	3.93
2 K min^{-1}	Heating	CrV-CrM	49.2	− 2.10	10 K min^{-1}	Heating	CrV-CrM	49.6	− 2.00
		CrM-CrS	59.8	24.90			CrM-CrS	68.5	34.06
		CrS-SmC	100.3	− 143.44			CrS-SmC	100.1	− 142.29
		SmC-Izo	131.2	− 29.59			SmC-Izo	131.9	− 30.23
	Cooling	Izo-SmC	130.6	25.53		Cooling	Izo-SmC	129.7	28.37
		SmC-CrIII	89.4	83.48			SmC-CrIII	89.32	84.53
		CrIII–CrIV	46.2	2.25			CrIII-CrIV	46.1	2.45
		CrIV–CrV	20.4	4.53			CrIV-CrV	8.6	2.56
3 K min^{-1}	Heating	CrV-CrM	49.5	− 2.83					
		CrM-CrS	60.4	21.91					
		CrS-SmC	99.9	− 142.39					
		SmC-Izo	131.4	− 28.65					
	Cooling	Izo-SmC	130.3	26.88					
		SmC-CrIII	89.2	83.77					
		CrIII-CrIV	46.3	2.21					
		CrIV-CrV	19.1	4.15					

(T_p-peak temperature) (cycle g)

This may suggest, that the sample left for 40 days at room temperature obtained its initial crystal phase order.

POM analysis

We recorded the textures of the phases during heating and cooling with a temperature change rate of 2 K min^{-1}. the sample was placed in a measuring cell 6 μm thick. Photos of textures are presented in Figs. 5 and 6. The registration of textures was consistent with the cycle b) of DSC tests (Fig. 2).

The texture of the CrM phase obtained during the heating of the 16OB sample (according to cycle b, Fig. 2) shows clear transverse "cracks" (Fig. 5), which are characteristic for glass phases present in liquid crystal materials [42]. During cooling, the textures of the crystalline phases

(CrIII, CrIV and CrV) are very similar and it is impossible to distinguish the phases by observing the textures.

TLI analysis

The measurements of the transmitted light intensity (TLI) are shown in Fig. 7a during heating and Fig. 7b during cooling, respectively. In this figures, we can observe transitions to: CrS phase, SmC phase and isotropic phase (during heating), and transition to SmC phase and crystallization (during cooling). Low energy transitions identifiable in DSC in the TLI method are invisible.

FTIR study

Fourier transform infrared spectroscopy is a good tool to identify phase transitions, even very subtle ones associated
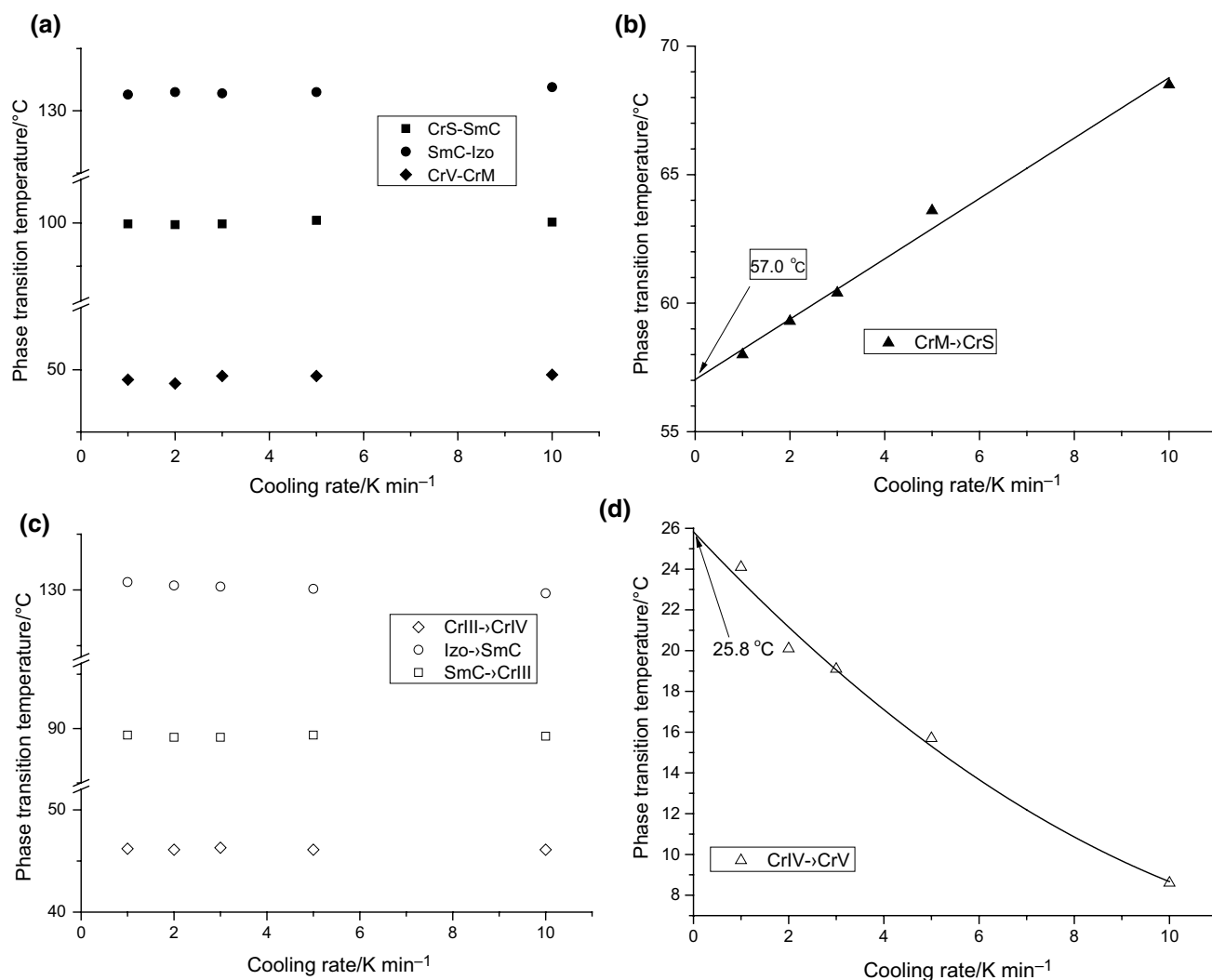
Fig. 3 Dependence of phase transition temperatures on the rate of temperature changes: **a** heating CrV→CrM, CrS→SmC and SmC→Izo; **b** heating: CrM→CrS; **c** cooling: Izo→SmC, SmC→CrIII and CrIII→CrIV; **d** cooling CrIV→CrV

with minor structural changes caused, for example, by van der Vaal's forces. The changes affect the dynamics of vibrations and are analysed by changing the parameters of the absorption bands of individual functional groups, especially the stretching vibrations of the carbonyl group ν(C=O).

We performed FTIR 16OB measurements as a function of temperature. Spectra were recorded according to DSC measurement cycles at 2 K min^{-1} (Fig. 2). We focused mainly on three spectral ranges:

– Carbonyl stretching area ν(C=O) in the range 1560–1760 cm^{-1}.
– Stretching area of ether ν(C–O–C$_{ar}$) and ν(C–O) carboxylic ethers groups in the range of 1110–1370 cm^{-1}.

– Aromatic bending area δ(C$_{ar}$–H) outside the plane in the range of 750–870 cm^{-1}.
– Selected IR spectra of the carbonyl group stretching vibrations corresponding to individual phases in 16OB during cooling and heating are shown in Fig. 8.

In the area of the stretching vibrations of the carbonyl group ν(C=O) in the crystalline phases of the "fresh" sample, a doublet is visible with the maxima at 1672 cm^{-1} and 1689 cm^{-1}, respectively (Fig. 8), which may indicate the presence of CrI and CrII multimeric structures involving hydrogen bonds. The parameters of the ν(C=O) bands in the CrI and CrII phases are almost the same. Based on the characteristics of the bands in both phases, it is not possible

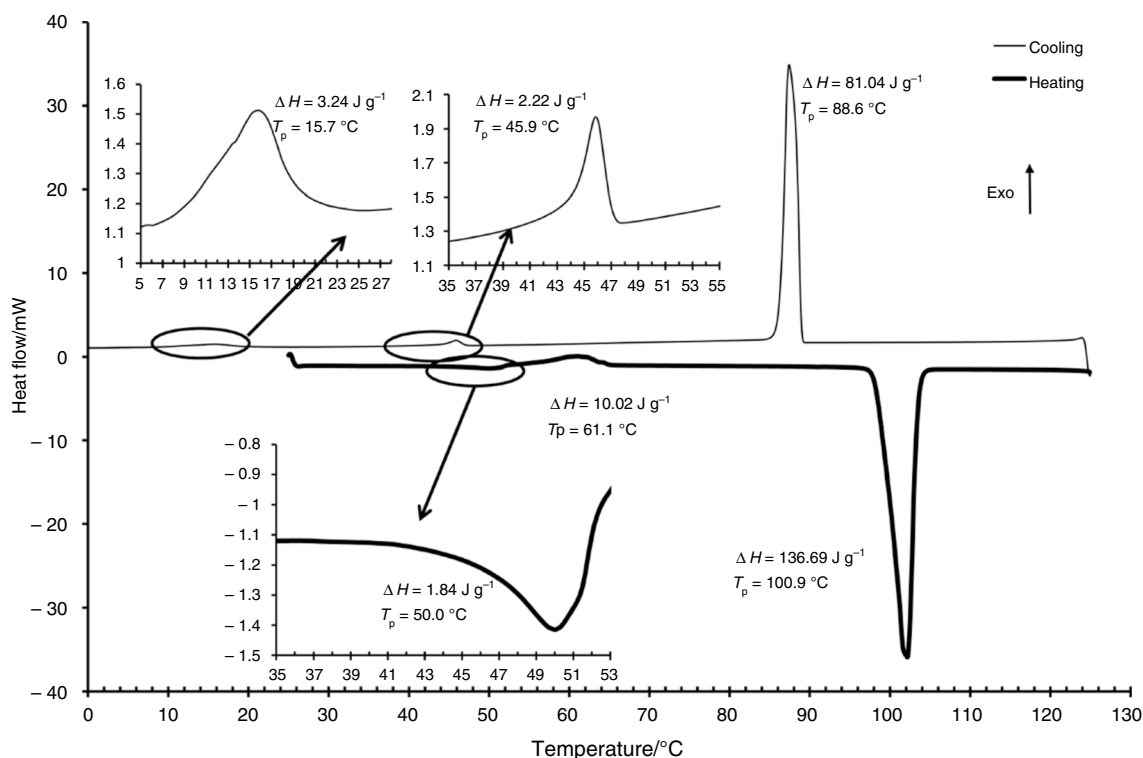**Fig. 4** DSC curve for 16OB taken after the sample has been at room temperature for 17 days since the last measurement
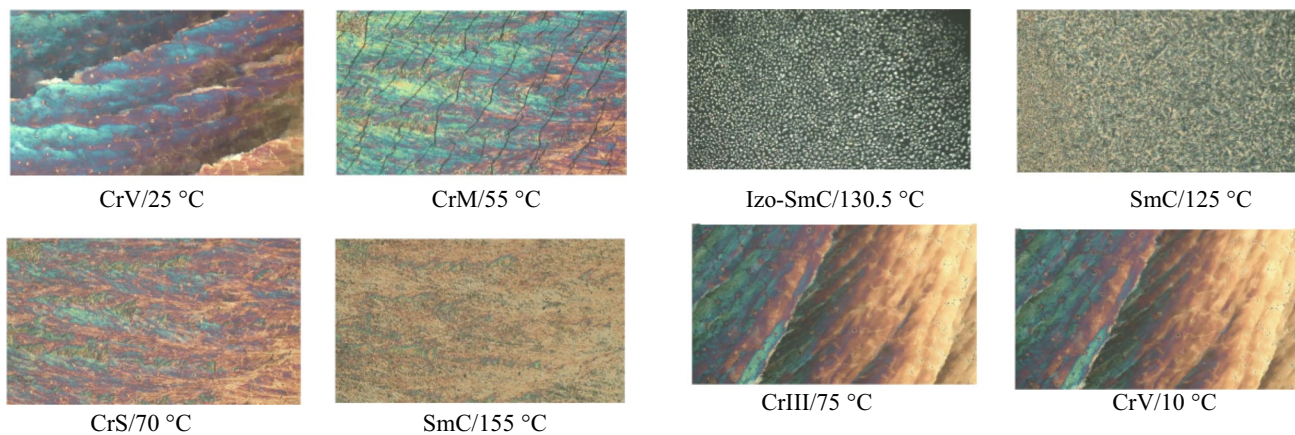

Fig. 5 The 16OB phase textures obtained during heating from −10 to 150 °C (2 K min⁻¹)

Fig. 6 The 16OB phase textures obtained during cooling from 150 to −10 °C (2 K min⁻¹)

to identify the CrI→CrII transition, which proves the high structural similarity of these phases. After melting the 16OB sample, the band characteristics changed, the doublet disappears and a single v(C=O) band is visible at 1686 cm⁻¹ in the SmC phase and at 1690 cm⁻¹ in the isotropic phase. Moreover, in the isotropic phase at 1737 cm⁻¹ there is a

single low intensity band which proves the presence of a "free" carbonyl group when the interactions are released. The transitions Cr→SmC and SmC→Izo are distinguished. Cooling the SmC phase leads to the formation of the CrIII phase. In the area of the CrIII phase, the band of stretching vibrations of the C=O group is visible as a single one at 1678 cm⁻¹ with a slightly outlined shoulder at 1689 cm⁻¹. In
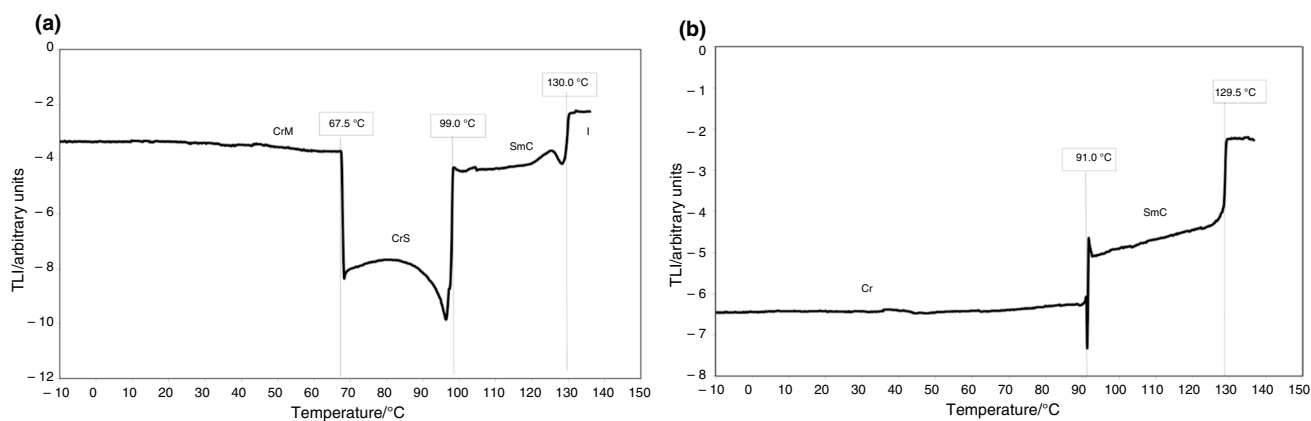
Fig. 7 TLI curve for 16OB obtained during: **a** heating and **b** cooling

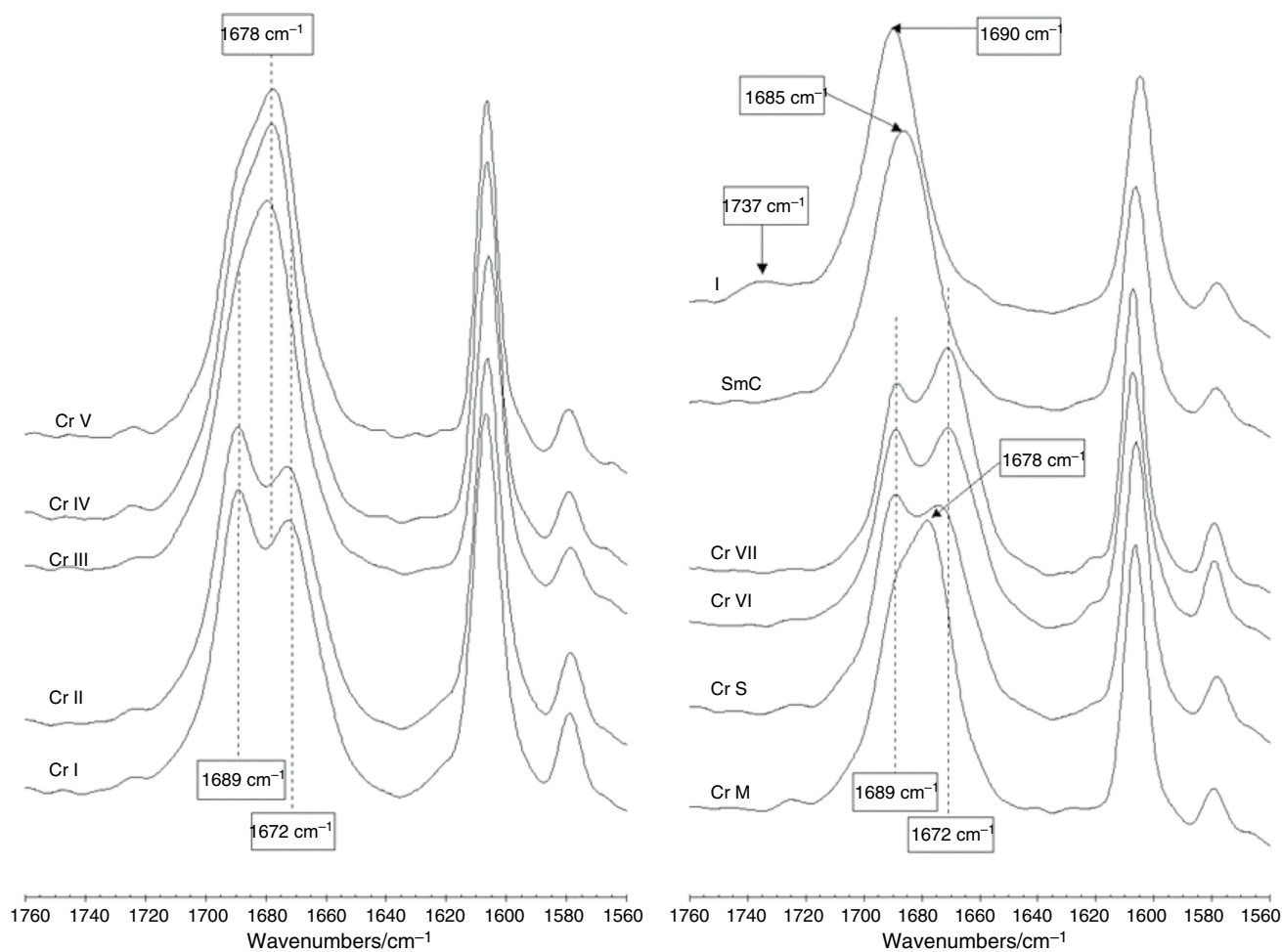**Fig. 8** The carbonyl stretching region of the infrared spectrum of 16OB

the CrIV and CrV phases, the characteristic of the $\nu(C=O)$ bands is similar to the $\nu(C=O)$ in CrIII, the difference is the outline of the band's shoulder, the lower the temperature of the phase, the clearer the outline. A change in the outline of

the C=O band shoulder and slight shifts towards a higher wavenumber may identify CrIII → CrIV → CrV phase transitions. In the CrM phase that occurs during the heating of the CrV phase, the $\nu(C=O)$ band at 1678 cm^{-1} retains a
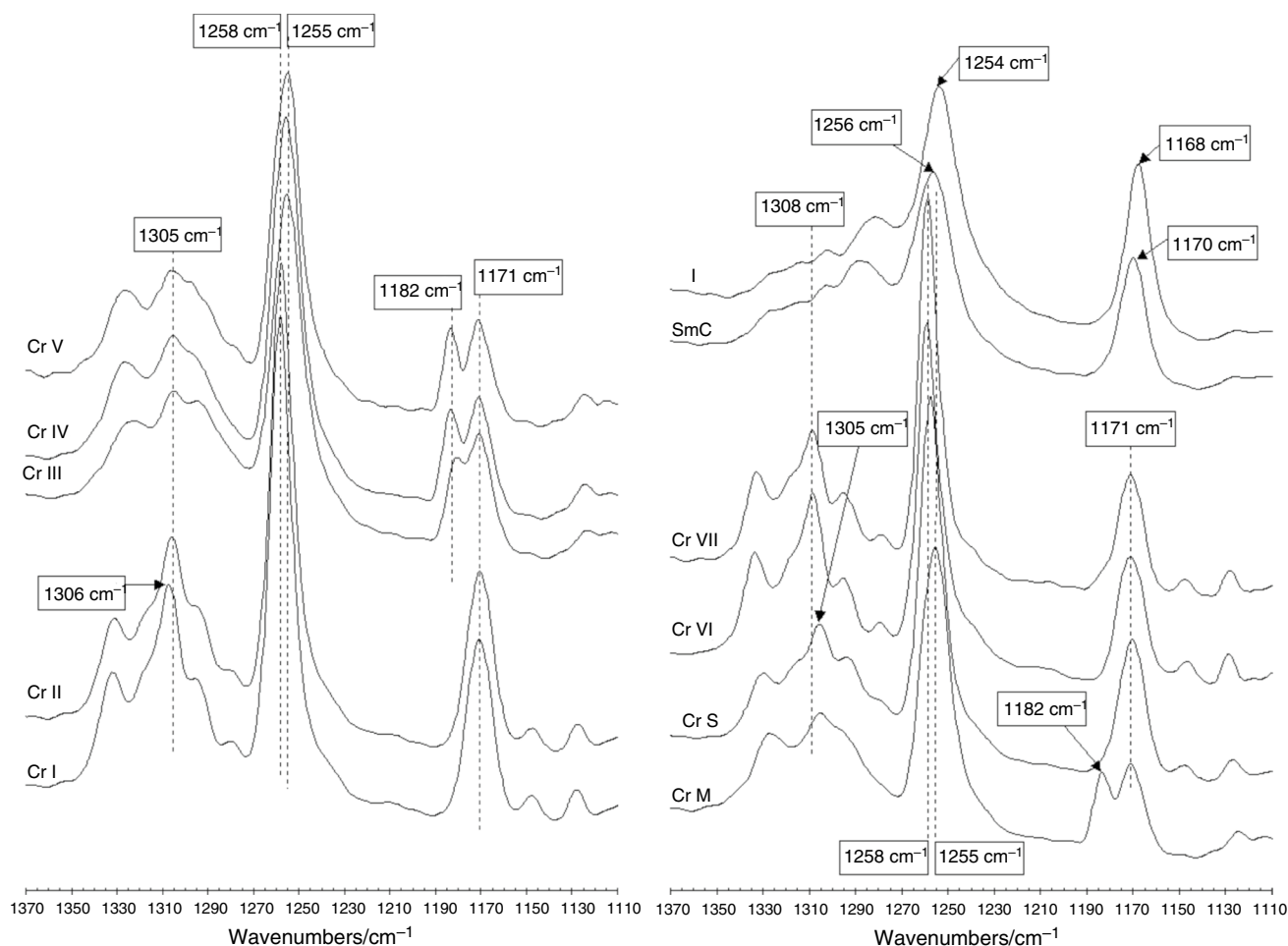
Fig. 9 The aromatic ν(C–O–CAr) ether and ν(C–O) carboxyl stretching region of the infrared spectrum of 16OB

shape very similar to the CrV phase, but with a clearly lower intensity (Fig. 8). The CrV → CrM phase transition (glass transition) can be identified by changing the intensity of the ν(C=O) band. In the CrS phase, formed during the heating of the CrM phase, the characteristic of the ν(C=O) band is different than in the CrM phase. Two maxima are visible, at 1672 cm^{-1} and 1689 cm^{-1}. The CrM → CrS transition is well identifiable by the FTIR method. The general characteristics of the ν (C=O) band in the CrS phase are preserved in the CrVI phase formed during the cooling of the CrS phase and in the CrVII phase formed during the heating of the CrVI phase. There are slight differences in the intensities of the maximum. In the areas of existence of the CrS, CrVI and CrII phases, the bands of stretching vibrations ν(C=O) form doublets, differing in the intensity of the peaks, at 1672 cm^{-1} and 1689 cm^{-1}.

Other regions of the FTIR spectrum sensitive to structural changes in the crystalline phases are found in the wave number regions: at 1300–1130 cm^{-1} (ν(C–O–C$_{ar}$) and ν(C–O) carboxylic stretching vibrations) (Fig. 9) and at 900–750 cm^{-1} (vibrations bending beyond the δ(C$_{ar}$–H) plane (Fig. 10) These regions are sensitive to structural changes occurring, for example, after the vitrification process.

The parameters of the bands of stretching vibrations of the groups ν(C–O–C$_{ar}$) (1200–1350 cm^{-1}) and ν(C–O) (1100–1190 cm^{-1}) in the CrI and CrII phases are almost identical (Fig. 9). In the CrIII phase, the ν(C–O) band in the carboxyl group gives a doublet with a maximum at 1171 cm^{-1} and 1182 cm^{-1}, a sharp band of vibrations ν(C–O–C$_{ar}$) at 1255 cm^{-1}. Bands observable in the CrIV and CrV phases are characterized by similar parameters. In the CrM phase in the wavenumber range
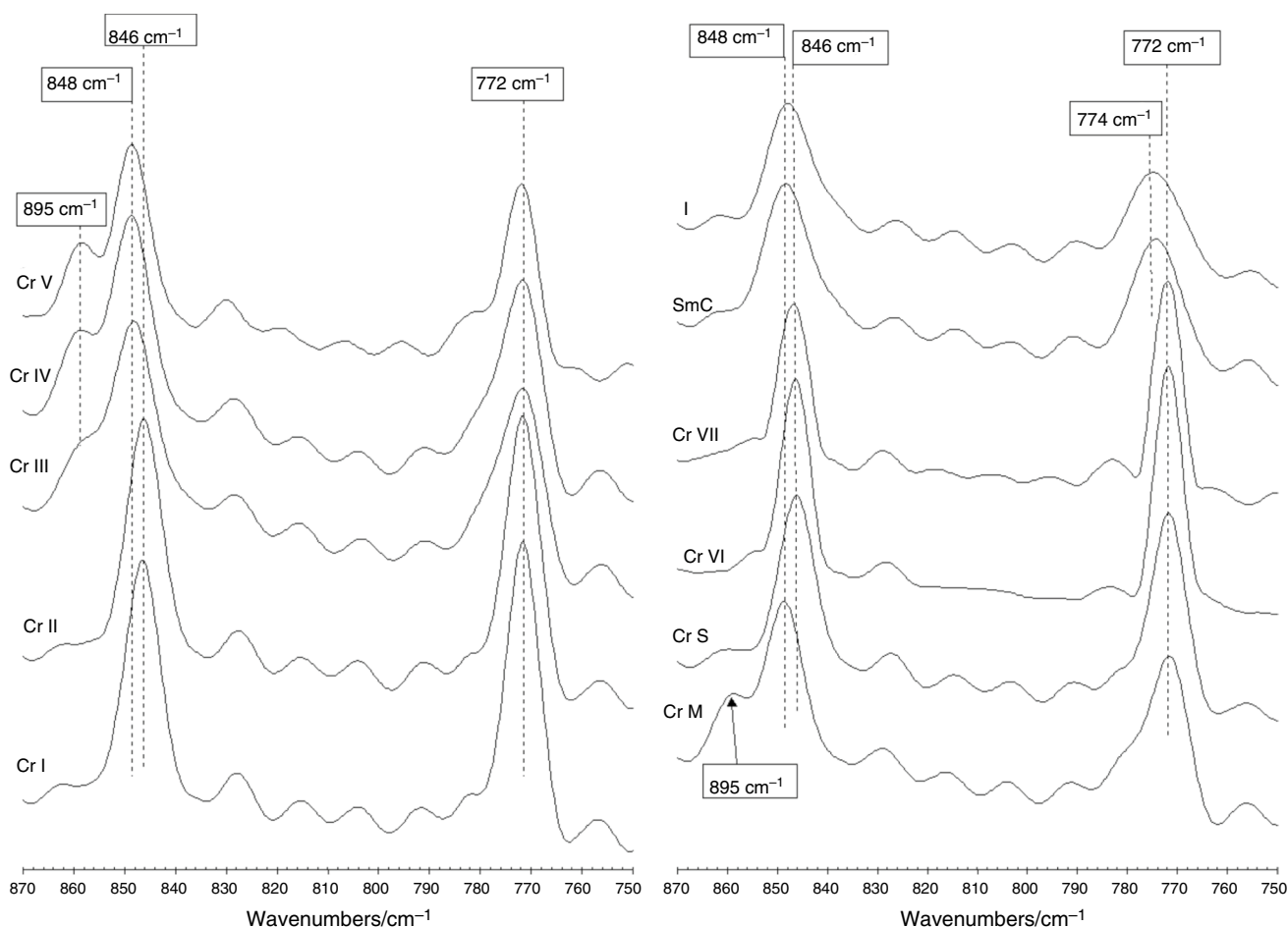
Fig. 10 The aromatic $\delta(C_{ar}–H)$ out-of-plane bending region of infrared spectrum of 16OB

1160–1190 cm^{-1} there is also a doublet, but its intensity is much smaller. The multiplet in the 1290–1350 cm^{-1} range is poorly scratched. In the CrS phase resulting from the exo-energetic effect, the $\nu(C–O)$ vibrations give a single band at 1171 cm^{-1}. The multiplet in the range of 1280–1350 cm^{-1} is clearly scratched from the maximum at 1305 cm^{-1}. Thus, it is possible to identify the CrM → CrS transition. The above shows that the areas of stretching vibrations $\nu(C–O–C_{ar})$ in the wave number range 1290–1350 cm^{-1} and $\nu(C–O)$ at 1160–1190 cm^{-1} are sensitive to structural changes taking place with the participation of hydrogen bonds after the vitrification process. The vibration area $\nu(C–O–C_{ar})$ in the 1240–1280 cm^{-1} area is basically insensitive to structural changes.

When analysing the area of aromatic bending vibrations $\delta(C_{ar}–H)$, a difference is noticeable in the parameters of the bands in the CrM and CrS phase in the wave

numbers range 840–900 cm^{-1} and 760–790 cm^{-1}. In the CrM phase, the band at 849 cm^{-1} has a clearly defined shoulder with a maximum at 896 cm^{-1}, which is not present in the CrS phase. The band at 772 cm^{-1} in the CrM phase is characterized by greater half-width (FWHM) and lower intensity than in CrS. The identification of the CrM–CrS transition is therefore also possible in the area of aromatic bending vibrations $\delta(C_{ar}–H)$. There is also a difference in the characteristics of the $\delta(C_{ar}–H)$ band at 895 cm^{-1} between the CrIII and CrIV phases (Fig. 10).

Changes in the parameters of the absorption bands $\nu(C=O)$ and $\nu(C–O)$ carboxyl recorded in FTIR spectra are related to structural changes resulting from non-covalent interactions. The formation of various structures with the participation of hydrogen bonds is possible [32]. Changes in the area of bending vibrations $\delta(C_{ar}–H)$ suggest that structures involving aromatic hydrogen atoms may be formed (Fig. 11).
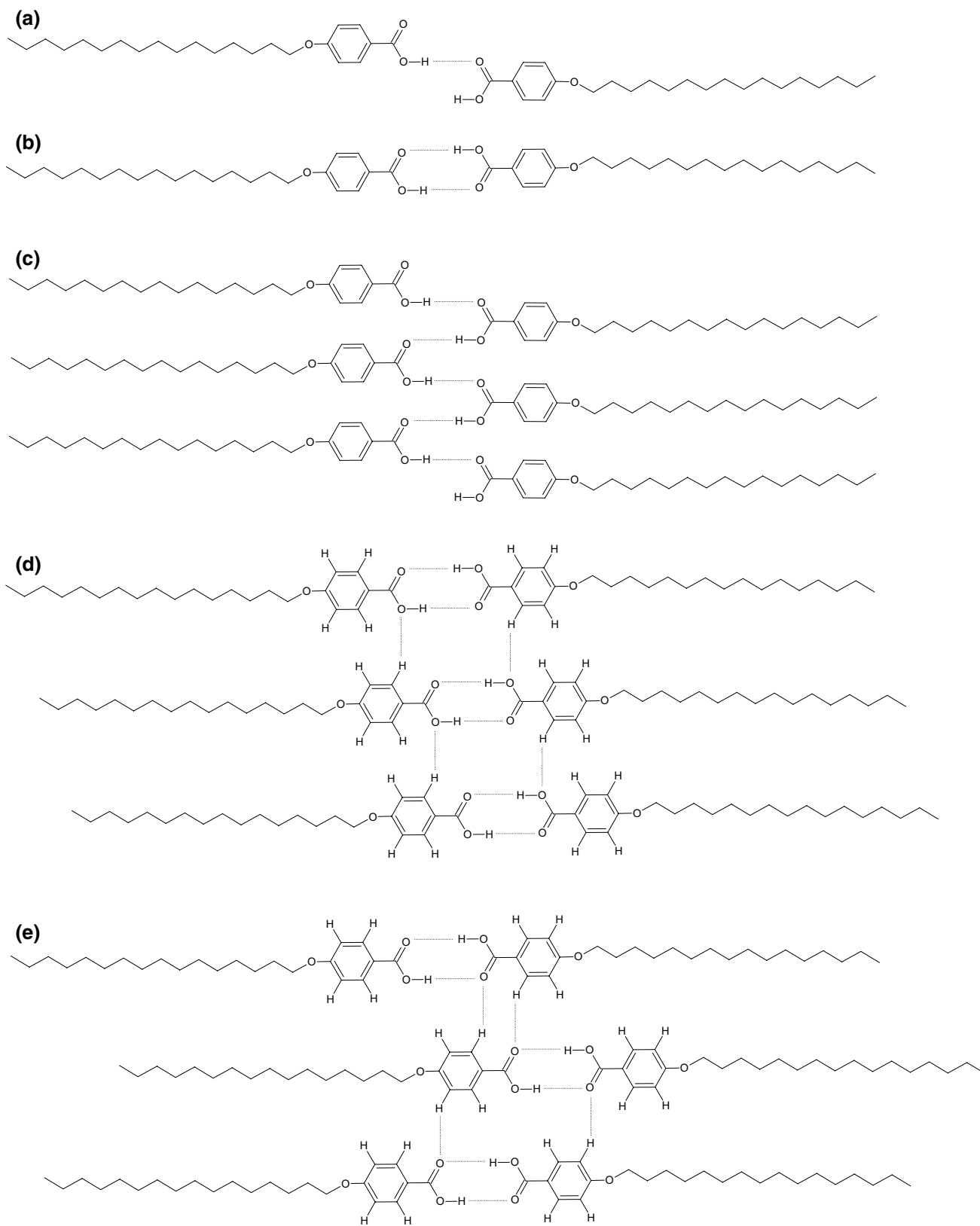
(a)

(b)

(c)

(d)

(e)

Fig. 11 Schematic representation of the hydrogen bonded dimmers and multimers in different 16OB phases

The quantum–mechanical calculations performed for a single molecule and its closed dimer at the lowest energy level (Fig. 1), show that very small energy pulses may cause a change in the angle of the molecules, break the hydrogen bond, and switch to an open dimer. The open dimer has the ability to create new intermolecular hydrogen bonds with the creation of long chain structures resembling polymer systems (Fig. 11).

Conclusions

From carried out studies it results:

1. 4-haxadecyloxy benzoic acid (16OB) is characterized by the presence of the enantiotropic SmC phase and the polymorphism of the crystalline phases.
2. The presence of an exo-energetic effect during heating is characteristic.
3. The DSC method is very consistent with the FTIR method. However, in the FTIR method, transitions between phases with a very similar structure are not noticeable and they are identifiable by the DSC method (e.g. CrI–CrII and CrIV–CrV)
4. The analysis of FTIR spectra as temperature function shows that the exothermic effect during heating is connected to the transition between phases: metastable and stable.
5. From FTIR spectra and calorimetric data it occurs that CrIII, CrIV, CrV and CrM are metastable phases. Remaining crystalline phases (CrI, CrII, CrVI, CrVII, CrS) are stable.
6. Metastable phases can exist at room temperature for a long time.
7. The FTIR tests show that dimer systems occur in liquid phases. The structure of closed dimers dominates in the SmC phase (Fig. 11b)), while in the isotropic phase, open dimers dominate (Fig. 11a).
8. We assume the existence of chain structures in the metastable phases (Fig. 11c). The multimeric structure shown in Fig. 11d) may also be present in a minor amount.
9. In the stable phases, the multimeter structure shown in Fig. 11e) is dominant.

Declarations

References

1. Demus D, Demus H, Zaszchke H. Flussige kristalle in tabelen. Leipzig: Veb Deutscher Verlag fur Grundstoffindustrie; 1974.
2. Plass M. Hydrogen bonding in liquid crystalline phase of *p–n*-alkoxybenzoic acids. Z Phys Chem. 1996;194:223–30. https://doi.org/10.1524/zpch.1996.194.Part_2.223.
3. Subhapriya P, Sadasivam K, Madhu Mohan MLN, Vijayanand PS. Experimental and theoretical investigation of *p–n* alkoxy benzoic acid based liquid crystals - a DFT approach. Spectrochim Acta A Mol Biomol Spectrosc. 2014;123:511–23. https://doi.org/10.1016/j.saa.2014.01.074.
4. Das P, Praveen PL. Structure and phase behavior of alkoxy benzoic acids in DMSO for thermodynamic applications: theoretical investigation. J Mol Struct. 2021;1233:130137. https://doi.org/10.1016/j.molstruc.2021.130137.
5. Giricheva NI, Syrbu SA, Bubnova KE, Fedorov MS, Kiselev MR, Girichev GV. H-complexes in the "4-n-alkoxybenzoic acid: 4-pyridyl 4′-n-alkoxybenzoate" system. IR spectroscopy and quantum chemical calculations. J Mol Liq. 2019;277:833–42. https://doi.org/10.1016/j.molliq.2019.01.029.
6. Kuzmina LG, Kucherepa NS, Pestov S, Kochetov AN. Molecular and crystal structure of 4-alkoxybenzoic acids: design of the mesogenic phase. Crystallogr Rep. 2009;54:862–79. https://doi.org/10.1134/S1063774509050204.
7. Al-Mutabagani LA, Alshabanah LA, Naoum MM, Hagar M, Ahmed HA. Experimental and computational approaches of newly polymorphic supramolecular H-Bonded liquid crystal complexes. Front Chem. 2020;8:571120. https://doi.org/10.3389/fchem.2020.571120.
8. Ely F, Conte G, Merlo AA, Gallardo H. A new synthetic approach based on (2)-menthone for chiral liquid crystals. Liq Cryst. 2004;31:1413–25. https://doi.org/10.1080/0267829041233129340.
9. Ossowska-Chruściel MD. A convenient synthesis and the mesomorphic properties of new chiral ferroelectric thiobenzoates. Liq Cryst. 2004;31:1159–65. https://doi.org/10.1080/02678290410001724764.
10. Ossowska-Chruściel MD, Roszkowski P, Rudzki A, Chruściel J. The influence of terminal chlorine on the mesomorphic properties of new thiobenzoates. Liq Cryst. 2005;32:877–87. https://doi.org/10.1080/02678290500125509.
11. Alhaddad OA, Abu Al-Ola KA, Hagar M, Ahmed HA. Chair- and V-shaped of h-bonded supramolecular complexes of azophenyl nicotinate derivatives; mesomorphic and DFT molecular

geometry aspects. Molecules. 2020;25:1510. https://doi.org/10.3390/molecules25071510.

12. Podruczna M, Hofmańska A, Niezgoda I, Pociecha D, Galewski Z. Influence of terminal groups on liquid-crystalline polymorphism of selected azobenzene derivatives. Liq Cryst. 2014;41:113–25. https://doi.org/10.1080/02678292.2013.839834.

13. Meco-Navas A, Ebiloma GU, Martín-Domínguez A, Martínez-Benayas I, Cueto-Díaz EJ, Alhejely AS, Balogun EO, Saito M, Matsui M, Arai N, Shiba T, Harada S, de Koning HP, Dardonville C. SAR of 4-alkoxybenzoic acid inhibitors of the trypanosome alternative oxidase. ACS Med Chem Lett. 2018;9(9):923–8. https://doi.org/10.1021/acsmedchemlett.8b00282.

14. Vijayakumar VN, Murugadass K, Madhu Mohan MLN. Inter hydrogen bonded complexes of hexadecylaniline and alkoxy benzoic acids : a study of crystallization kinetics. Braz J Phys. 2009;39:600–5. https://doi.org/10.1590/S0103-97332009000500017.

15. Tejaswi M, Pardhasaradhi P, Madhav BTP, Pandian K, Jayaprada P, Manepalli RKNR, Pisipati VGKM. Optical properties of liquid crystalline alkoxy benzoic acids with dispersed citrate-capped gold nanoparticles. Z Naturfor A. 2019;74:1001–22. https://doi.org/10.1515/zna-2019-0100.

16. Zalewski S. Phase transitions in three-components mixture containing alkoxy benzoic acids with a chiral material. Phase Trans. 2019;92:1102–9. https://doi.org/10.1080/01411594.2019.1689569.

17. Patari S, Nath A. Tunable dielectric and conductivity properties of two 4-n alkoxy benzoic acid. Opto-Electron Rev. 2018;26:35–43. https://doi.org/10.1016/j.opelre.2017.12.002.

18. Kanuga K. Degradation of polyester film exposed to accelerated indoor damp heat aging. In Conference record of the 2011 37th IEEE photovoltaic specialists conference, 19–24 June 2011. https://doi.org/10.1109/PVSC.2011.6185853

19. Tsuji H, Bouapao L. Stereocomplex formation between poly(L-lactic acid) and poly(D-lactic acid) with disproportionately low and high molecular weights from the melt. Polym Int. 2012;61:442–50. https://doi.org/10.1002/pi.3219.

20. Shyr TW, Tung CH, Cheng WS, Yang CC. The crystallization rate and morphological structure of poly(ethylene/trimethylene terephthlate) copolyesters under isothermal melt-crystallization and cold-crystallization. J Polym Res. 2013;20:186. https://doi.org/10.1007/s10965-013-0186-5.

21. Henricks J, Boyum M, Zheng W. Crystallization kinetics and structure evolution of a polylactic acid during melt and cold crystallization. J Therm Anal Calorim. 2015;120:1765–74. https://doi.org/10.1007/s10973-015-4460-0.

22. Lu H, Nutt S. Cold-crystallization kinetics of syndiotactic polystyrene. J Appl Polym Sci. 2003;89:3464–70. https://doi.org/10.1002/app.12559.

23. Kolek Ł, Massalska-Arodź M, Adrjanowicz K, Rozwadowski T, Dychton K, Drajewicz M, Kula P. Molecular' dynamics and cold crystallization process in a liquid-crystalline substance with para-, ferro- and antiferro-electric phases as studied by dielectric spectroscopy and scanning calorimetry. J Mol Liq. 2020;297:111913. https://doi.org/10.1016/j.molliq.2019.111913.

24. Jasiurkowska-Delaporte M, Rozwadowski T, Dmochowska E, Juszynska-Gałązka E, Kula P, Massalska-Arodź M. Interplay between crystallization and glass transition in nematic liquid crystal 2,7-bis(4-pentylphenyl)-9,9-diethyl-9H- fluorene. J Phys Chem B. 2018;122:10627–36. https://doi.org/10.1021/acs.jpcb.8b08138.

25. Drzewicz A, Juszyńska-Gałązka E, Zając W, Kula P. Vibrational dynamics of a chiral smectic liquid crystal undergoing vitrification and cold crystallization. Crystals. 2020;10:655. https://doi.org/10.3390/cryst10080655.

26. Rozwadowski T, Massalska-Arodź M, Kolek Ł, Grzybowska K, Bak A, Chłędowska K. Kinetics of cold crystallization of 4-cyano-3-fluorophenyl 4-butylbenzoate (4CFPB) glass forming liquid crystal. I. Nonisothermal process as studied by microscopic, calorimetric, and dielectric methods. Cryst Growth Des. 2015;15:2891–900. https://doi.org/10.1021/acs.cgd.5b00328.

27. Efimova A, Hubrig G, Schmidt P. Thermal stability and crystallization behavior of imidazolium halide ionic liquids. Thermochim Acta. 2013;573:162–9. https://doi.org/10.1016/j.tca.2013.09.023.

28. Sampath S, Boopathi AA, Mandal AB. "Bottom-up" selfassembly and 'cold crystallization' of butterfly shaped tetrabenzofluorene molecules. Phys Chem Chem Phys. 2016;18:21251–8. https://doi.org/10.1039/C6CP02662A.

29. Iwase K, Toyama Y, Yoshikawa I, Yamamura Y, Saito K, Houjou H. Insight into structural demand for cold crystallization of a small molecule. A case study for schiff base compounds that exhibit prototropic tautomerization. Bull Chem Soc Jpn. 2018;91:669–77. https://doi.org/10.1246/bcsj.20170386.

30. Iwase K, Nagano Y, Yoshikawa I, Houjou H, Yamamura Y, Saito K. Cold crystallization in schiff-base nickel(II) complexes derived from three toluidine isomers. J Phys Chem C. 2014;118:27664–71. https://doi.org/10.1021/jp5081516.

31. Ossowska-Chruściel MD, Korlacki R, Kocot A, Wrzalik R, Chruściel J, Zalewski S. Infrared study of orientational order parameters of a ferroelectric liquid crystal. Phys Rev E. 2004;70:041705. https://doi.org/10.1103/PhysRevE.70.041705.

32. Painter P, Cleveland C, Coleman M. An infrared spectroscopic study of p–n-alkoxybenzoic acids. Mol Cryst Liq Cryst. 2000;348:269–93. https://doi.org/10.1080/10587250008024811.

33. Kuzmina LG, Kucherepa NS, Pestov S. Molecular and crystal structure of 4-alkoxybenzoic acids: design of the mesogenic phase. Crystallogr Rep. 2009;54:862–79. https://doi.org/10.1134/S1063774509050204.

34. Zhang H, Jakisch L, Komber H, Voit B, Böhme F. Synthesis of multifunctional coupling agents and their selective reactions with hydroxy and amino groups in the melt. Tetrahedron. 2013;68:3656–4366. https://doi.org/10.1016/j.tet.2013.03.024.

35. TURBOMOLE, V7.3; A Development of University of Karlsruhe and Forschungszentrum Karlsruhe GmbH, 1989–2007. TURBOMOLE GmbH: Karlsruhe, Germany, 2018. Available online: http://www.turbomole.com (Accessed on 7 Jul 2020).

36. Weigend F, Ahlrichs R. Balanced basis sets of split valence, triple zeta valence and quadruple zeta valence quality for H to Rn: design and assessment of accuracy. Phys Chem Chem Phys. 2005;7:3297–305. https://doi.org/10.1039/B508541A.

37. Stephens PJ, Devlin FJ, Chabalowski CF, Frisch MJ. Ab initio calculation of vibrational absorption and circular dichroism spectra using density functional force fields. J Phys Chem. 1994;98:11623–7. https://doi.org/10.1021/j100096a001.

38. Caldeweyher E, Bannwarth C, Grimme S. Extension of the D3 dispersion coefficient model. J Chem Phys. 2017;147:034112. https://doi.org/10.1063/1.4993215.

39. Chruściel J, Zalewski S, Ossowska-Chruściel MD, Filiks A, Rudzki A. Transmission optical methods. In: Mikuli E, Mikuli A, editors. Complementary methods of phase transformation studies. Jagiellonian University; 2006. pp. 255.

40. Drzewicz A, Jasiurkowska-Delaporte M, Juszyńska-Gałązka E, Zając W, Kula P. On the relaxation dynamics of a double glass-forming antiferroelectric liquid crystal. Phys Chem Chem Phys. 2021;23:8673–88. https://doi.org/10.1039/D0CP06203K.

41. Juszyńska-Gałązka E, Zieliński PM, Massalska-Arodź M, Krawczyk J. Solid state polymorphism and dynamics of 2,2-dimethylbutan-1-ol as studied by adiabatic calorimetry and dielectric spectroscopy. Acta Phys Polon A. 2013;124(6):917–25. https://doi.org/10.12693/APhysPolA.124.917.

42. Kolek Ł, Massalska-Arodź M, Majda D, Suchodolska B, Zalewski S. Studies of phase diagram and glass transitions of a liquid crystal with ferro- and antiferroelectric phases. Acta Phys Polon A. 2013;124(6):909–12. https://doi.org/10.12693/APhysPolA.124.909.